Helical beating of an actuated elastic filament

2009 J. Phys.: Condens. Matter 21 204109

(http://iopscience.iop.org/0953-8984/21/20/204109)

IOP PUBLISHING JOURNAL OF PHYSICS: CONDENSED MATTER

J. Phys.: Condens. Matter **21** (2009) 204109 (7pp) doi:10.1088/0953-8984/21/20/204109

Helical beating of an actuated elastic filament

Naïs Coq, Olivia du Roure, Marc Fermigier and Denis Bartolo

PMMH ESPCI ParisTech, CNRS UMR 7636, Université Pierre et Marie Curie, Université Denis Diderot, 10 rue Vauquelin 75231 Paris cedex 05, France

E-mail: nais.coq@espci.fr and denis.bartolo@espci.fr

Received 8 September 2008, in final form 23 October 2008
Published 21 April 2009
Online at stacks.iop.org/JPhysCM/21/204109

Abstract

We investigate the propulsive force resulting from the rotation of a flexible filament in the low Reynolds number regime. Using a simple linear model, we establish the nonlinear torque–force relations for two torque-driven actuation modes. When the rotation of the filament is induced by two perpendicular transverse oscillating torques, the propulsive force increases monotonically with the torque amplitude. Conversely, when a constant axial torque is applied, the torque–force characteristics displays an unstable branch, related to a discontinuous transition in the shape of the filament. We characterize this shape transition using two geometrical parameters, quantifying the wrapping around and the collapse on the axis of the filament. The proposed theoretical description correctly accounts for our experimental observations and reveals a strong dependence of the filament dynamics on the anchoring conditions.

(Some figures in this article are in colour only in the electronic version)

1. Introduction

The oscillation of flexible flagella and the rotation of 'rigid' chiral arms are the two standard propulsion strategies used by microorganisms [1]. The hydrodynamics of these two modes of locomotion have been extensively studied in the past, both theoretically and experimentally (see, e.g., [2, 3] and references therein). Recently, Dreyfus *et al* succeeded in fabricating the first human-made microswimmer, relying on the magnetic actuation of an artificial flagellum made of self-assembled paramagnetic colloids [4]. Conversely, the design of chiral propelling microstructures remains a technical challenge. A possible solution to this problem could be the use of soft rotating filaments which spontaneously adopt chiral shapes.

In this paper we focus on this intermediate propulsion mechanism, which has attracted much interest in the last two years and motivated a set of theoretical, numerical and experimental works [5–8]. Here we combine a theoretical and experimental study to extend the elastohydrodynamics description we proposed in [8]. Firstly, on the basis of a simple linear model, we establish the nonlinear constitutive relations between the propulsive force and the actuation torques. We show important qualitative differences between two beating modes in torque-driven systems. The propulsive force increases monotonically with the torque amplitude in the case of two transverse torques applied perpendicularly on the filament (figure 1(A)). In contrast, elastic filaments actuated by a constant longitudinal torque (figure 1(B)) exhibit an unstable branch in the force–torque relation, which can lead to a strong discontinuity in the propulsion force when the rotation period becomes of the order of the largest relaxation time of the bending modes. Secondly, we present an extended analysis of our experiment performed with a macroscopic flexible filament immersed in a viscous fluid. Force and torque measurements are in excellent agreement with our simple model. Furthermore, our observations allow us to relate the strong nonlinearities in the force response to a wrapping transition in the shape of the filament.

2. Force–torque constitutive relations for a rotating flexible filament

2.1. Beating of flexible rods: a minimal model

The beating of flexible rods in viscous flows has proven to be accurately described by simple models ignoring geometric nonlinearities and nonlocal hydrodynamic effects [9, 10]. We here restrict our analysis to this framework. More precisely, we consider a flexible rod initially straight and oriented

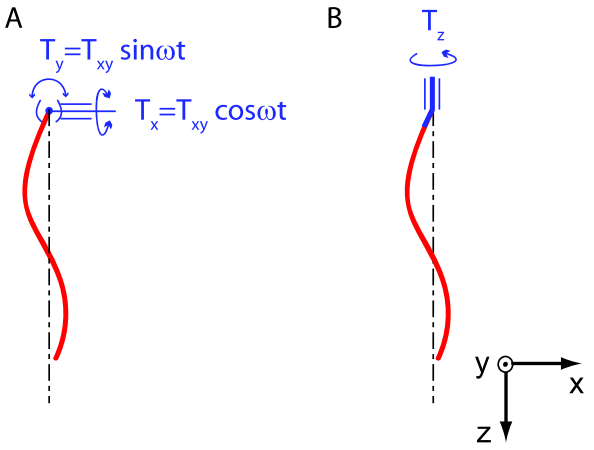

Figure 1. (A) Sketch of a flexible filament actuated by two AC transverse perpendicular torques oriented along the x and y axes. (B) Sketch of the same filament actuated by a DC axial torque oriented along the z axis.

with an angle ψ with respect to the rotation axis z. The rotation of the filament is imposed at one of its extremities ($z = 0$), while the other end remains free ($z = L$) (figure 2). The external torques applied at the anchoring point impose the rotation of the tangent vector: $\mathbf{t}(0, t) = [\psi \cos(\omega t), \psi \sin(\omega t), 1]$. As a result of the competition between viscous and elastic forces, the filament adopts a curved shape, $\mathbf{r} = [x(z), y(z), z]$, parametrized by the z coordinate. Within the small deformations approximation the bending energy of the rod is a quadratic function of its local curvature $|\partial_z^2 \mathbf{r}|$: $E_{\mathrm{el}} = \frac{1}{2}\int \mathrm{d}z\, \kappa (\partial_z^2 \mathbf{r})^2$, the resulting local elastic force being $\mathbf{f}_{\mathrm{el}} = -\kappa \partial_z^4 \mathbf{r}$. The coupling with the surrounding viscous fluid is modeled by a local anisotropic friction coefficient (resistive force theory). The local viscous drag is defined by

$$\mathbf{f}_{\mathrm{v}} = (\eta_{\parallel} - \eta_{\perp})(\mathbf{t} \cdot \mathbf{v})\mathbf{t} + \eta_{\perp}\mathbf{v}, \tag{1}$$

where $\mathbf{v}$ is the material velocity and $\eta_{\parallel}$ and $\eta_{\perp}$ are the longitudinal and transverse drag coefficients, respectively. These coefficients are approximated by their values for a straight slender rod with a circular cross section: $\eta_{\perp} = 4\pi\eta/[\log(L/a) + \frac{1}{2}]$ and $\eta_{\parallel} = 2\pi\eta/[\log(L/a) - \frac{1}{2}]$, where a is the radius of the rod and η is the viscosity of the fluid [11]. In the small deformations approximation, the force balance equation $\mathbf{f}_{\mathrm{e}} + \mathbf{f}_{\mathrm{v}} = 0$ reduces to the so-called Machin equation [12]:

$$\eta_{\perp}\partial_t \mathbf{r} = -\kappa \partial_z^4 \mathbf{r}. \tag{2}$$

After a spatial Fourier transform, this equation is readily solved. The rod undergoes a rigid body rotation at angular frequency ω as a result of the superposition of four propagating bending waves damped over a distance

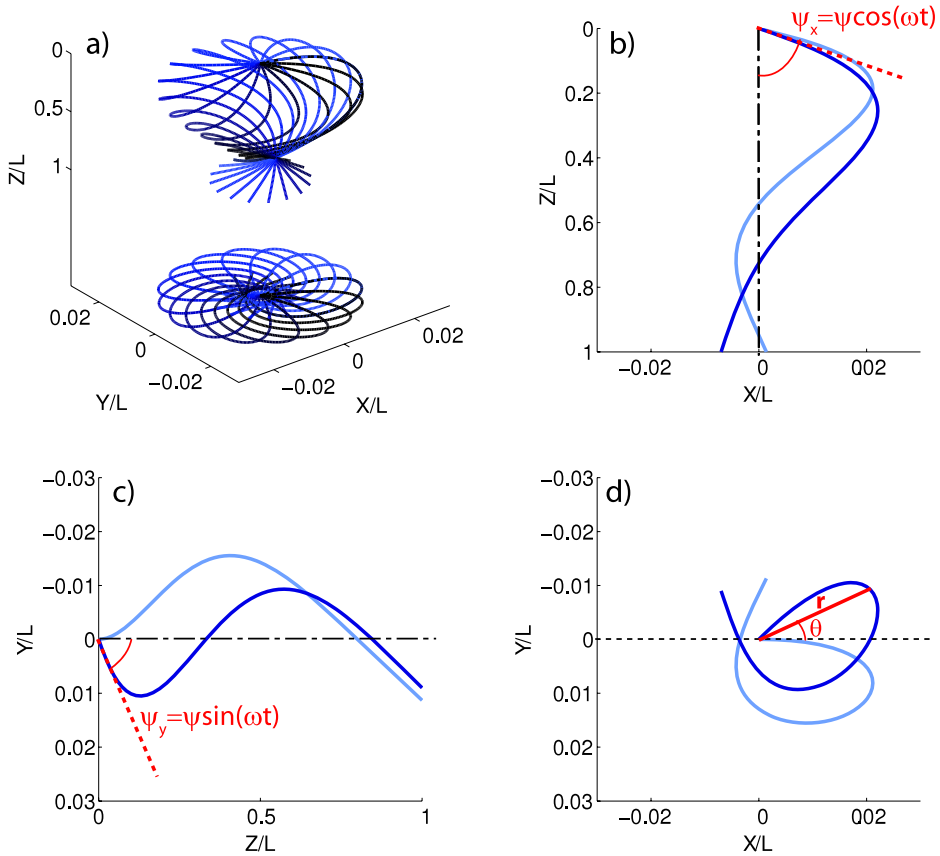

Figure 2. Shape of an elastic filament driven at $z = 0$ for $l_\omega/L = 0.18$ and $\psi = 15°$, computed from equation (2). (a) Thirty snapshots of the filament profile over one rotation period. Below are their projections in the (x, y) plane. The time interval between each snapshot is constant. (b)–(d) Projection of the same two profiles in the (x, z), (y, z) and (x, y) planes, respectively, taken at two different times. Note that the filament undergoes a rigid body rotation although the projected shapes in the (x, z) and (y, z) planes are time dependent.

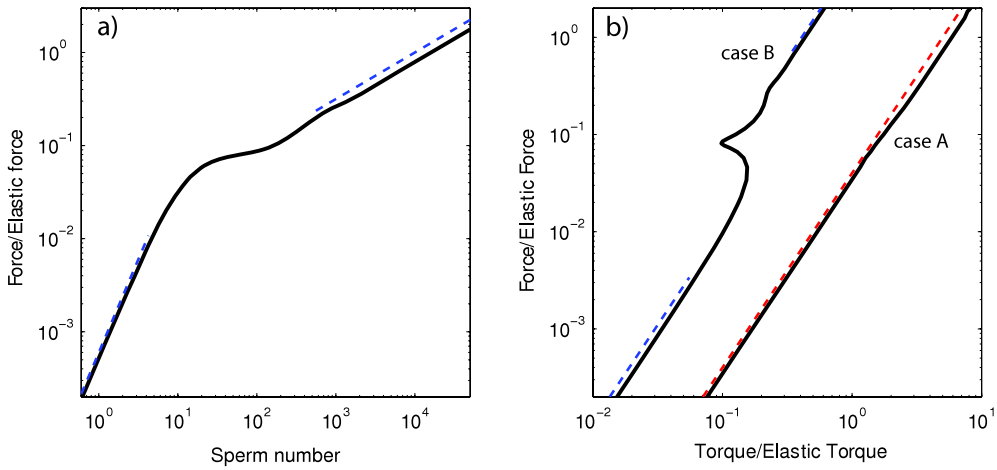

Figure 3. (a) Propulsive force normalized by the elastic force as a function of Sp. The force is computed as described in the text. Solid line: theoretical prediction from the linear model. Dashed lines: asymptotic scaling behaviors, Sp^2 and $Sp^{1/2}$ in the low and high Sp limits respectively. (b) Normalized propulsive force F_z/F_e versus normalized transverse torque T_{xy}/T_e (case A) and versus normalized axial torque T_z/T_e (case B), where the torques are computed from equation (5). Solid lines: theoretical predictions from the linear model. Dashed line for case A: quadratic power law. Dashed lines for case B: asymptotic scaling behaviors, T_z^2 in both the low and high T_z limits.

$l_\omega \equiv (\kappa/\eta_\perp\omega)^{1/4}$. Defining the four complex wavenumbers, $q_n(\omega) = l_\omega^{-1}\exp[\mathrm{i}(n\frac{\pi}{2} - \frac{\pi}{8})]$, the rod profile is given by

$$x(z,t) = (\psi L)\ \mathrm{Re}\left(\sum_{n=1}^{4}\alpha_n\, \mathrm{e}^{[\mathrm{i}\omega t - q_n(\omega)z]}\right), \tag{3}$$

$$y(z,t) = (\psi L)\ \mathrm{Im}\left(\sum_{n=1}^{4}\alpha_n\, \mathrm{e}^{[\mathrm{i}\omega t - q_n(\omega)z]}\right). \tag{4}$$

The α_n coefficients are set by the boundary conditions $\mathbf{r}(0) = 0$ (fixed end), $\partial_z(t) = \mathbf{t}(0,t)$ (angular actuation), $\partial_z^3\mathbf{r}(L) = 0$ (force free end) and $\partial_z^2\mathbf{r}(L) = 0$ (torque free end). A typical representation of these stationary chiral shapes is displayed in figure 2.

2.2. Propulsive force

We now focus on the propulsive properties of the filament. As the viscous flow bends the filament into a chiral shape, a nonzero thrust is generated along the z axis. The anchoring point experiences an axial force $F_z = \mathbf{e}_z \cdot \int \mathbf{f}_v(z)\,\mathrm{d}z$, with $\mathbf{f}_v$ as defined in equation (1). In all that follows, the forces are normalized by the elastic force necessary to bend the filament with a curvature of order $1/L$: $F_e \equiv \kappa/L^2$. We define a normalized rotation speed using the viscous relaxation time of the bending mode of wavelength L, $\tau = \eta_\perp L^4/\kappa$. The resulting dimensionless number, $Sp \equiv \omega\eta_\perp L^4/\kappa$, is commonly referred to as the Sperm number in the context of low Reynolds number locomotion; it may also be convenient to express Sp in terms of penetration length: $Sp = (L/l_\omega)^4$. The variations of the normalized axial force with the Sperm number are shown in figure 3(a). The axial force increases monotonically with the Sperm number; this increase is rather fast in the low Sp regime whereas it weakens for large Sp. To account for these variations, we stress that both the three-dimensional shape of the rotating filament and the axial force F_z are identical to those obtained by the superposition of two filaments beating periodically in perpendicular planes. Indeed, using equation (2) and the boundary conditions at the filament ends, one can easily provide a local expression for $F_z = \kappa(1 - \eta_\perp/\eta_\parallel)\sum_{u=x,y}[\partial_z u(0)\partial_z^3 u(0) - \frac{1}{2}\partial_z^2 u^2(z)]$, which is a well-known result in the context of planar oscillations [9]. It yields a thrust increasing quadratically with the beating pulsation ω in the low frequency limit. It is worth mentioning that this scaling law can also be predicted from a symmetry argument. At low Reynolds number, a rotating chiral object experiences a viscous force $F_z = M\omega$, where M is a coefficient of the so-called mobility matrix [13]. M is zero for a nonchiral object; since at $\omega = 0$ the filament is straight, $M(\omega = 0)$ must vanish. Moreover, changing the sign of the rotation changes the chirality of the filament, which implies that M is an odd function of ω. Hence, in the low-speed limit, we expect M to increase linearly with the angular velocity leading to an overall force proportional to ω^2. It follows that $F_z \sim F_e Sp^2$ from dimensional analysis. Note that this implies that the sign of the force is independent of the direction of rotation, as noticed in [5].

In the high Sp limit, the filament is strongly deformed. The chiral deformations are localized in a region of extent $l_\omega \ll L$ in the vicinity of the anchoring point. For $z > l_\omega$ the bending waves in both the (x,z) and (y,z) planes are damped and the filament has collapsed on the rotation axis. The force produced by the wrapped filament is comparable to the one induced by the rotation of a rigid helix of length, pitch and radius l_ω, which increases as ωl_ω^2. It then follows from dimensional analysis that $F_z \sim F_e Sp^{1/2}$ in this high Sp limit. Note that this last scaling argument holds beyond the small deformations approximation.

2.3. Torque controlled actuation: discontinuous dynamic transition

We have here characterized the propulsive force corresponding to a given beating pulsation, independently of the actuation

mechanism at the rod end. We now investigate two specific forcings where imposed external torques drive the filament. We show that major differences arise in the force–torque constitutive relation as well as in the filament kinematics.

The two actuations modes we consider (referred to here as A and B) are sketched in figure 1. In case A the rotation of the tangent vector at the anchoring point around the z axis results from the simultaneous periodic oscillations of two transverse torques (T_x and T_y) aligned along the x and y axis (see figure 1(A)). For sake of simplicity we only consider the case where the two torques have the same amplitude and a $\pi/2$ phase shift: $T_x = T_{xy}\cos(\omega t)$ and $T_y = T_{xy}\sin(\omega t)$. T_x and T_y alone would induce the propagation of planar deformations along the filament. In case B the rotation is induced by a constant torque T_z in the z direction applied to a crankshaft which sets the angle between the tangent vector and the rotation axis (see figure 1(B)).

Whatever the actuation mode, the external torque applied on the filament balances the local viscous torque integrated along the filament:

$$\mathbf{T} = -\int \mathbf{r} \times \mathbf{f}_v \, dz, \tag{5}$$

where the viscous force is defined in equation (1). We now establish the constitutive relations between the propulsive force F_z and the external torque amplitudes parametrized by the angular velocity ω. More precisely, we computed the torques $T_{xy}(\omega)$ or $T_z(\omega)$ required to rotate the filament at a given ω, knowing the filament shape from equations (3) and (4) and using equations (1) and (5).

Before giving a more detailed description, we can anticipate the asymptotic behaviors common to the two actuation modes. In the low Sp (low speed) limit the filament is barely deformed. The torque $\mathbf{T}$ is then simply the one needed to rotate a tilted rigid rod in a viscous fluid and both T_{xy} and T_z scale as $\eta_\perp \omega L^3 \sim Sp$. In the other limit, large Sp, only a portion of length l_ω deviates from the z axis, on a distance of order l_ω as well, and contributes to the viscous torque. As a consequence the rigid body rotation of such filaments collapsed on the z axis induces torques of typical amplitude $\eta_\perp \omega l_\omega^3 \sim Sp^{1/4}$ in the three directions. Combining these predictions with the asymptotic scalings for F_z, we infer that the axial force increases quadratically with the imposed torque amplitude whatever the actuation mode (A or B) both in the small and large torques limits: $F_z \sim T_{xy}^2$ for case A, and $F_z \sim T_z^2$ for case B. However, plotting the full constitutive relations, we uncover a major difference between the apparently similar actuation mechanisms (figure 3(b)). Again, torques are systematically normalized by the elastic torque $T_e = \kappa/L$. In case A, as expected, the axial force is a monotonically increasing function of T_{xy} as in the case of a 2D beating. More surprisingly the constitutive relation is very well approximated by a single quadratic function for all Sp. In case B, in contrast, this second actuation mode reveals a counter intuitive response to the axial torque. Indeed for intermediate torques (corresponding to intermediate Sperm numbers) F_z decreases with T_z. This decreasing branch is unstable and would lead in practice to hysteretic jumps in the axial force upon torque cycling. This result is in good agreement with the Brownian dynamics simulations of Manghi *et al* [5]. We wish to emphasize that this phenomenon is intrinsically related to the *nonlinear* interplay between the *linear* elasticity and the *linear* viscous flow. In the case of rotating rigid chiral structures the linearity of the Stokes equation implies that the axial force should increase linearly with the applied torque whatever the detailed shape of the objects.

From a design perspective, two specificities of such a flexible propeller are worth mentioning at this point. Firstly, the overall quadratic increase of the force with the actuation torque means that the range of available forces is wider when the chirality of the rotating body is induced by the fluid–structure interaction. Secondly, it follows from the constitutive relations that these two actuation modes obviously offer very different propulsion strategies. The case A mode, which requires two independent rotational actuators, provides very robust forces with respect to the torque fluctuations. Conversely, to vary its propulsive force over a wide dynamical range a swimmer using a case B actuation only needs slight modulations of its control torque.

3. Experiments: shape and force transitions

To better understand the counter intuitive response of the elastic filament to an external axial torque (case B), we performed a rotation speed controlled experiment on macroscopic flexible filaments. Firstly, our measurements allowed us to assess the validity of the predictions in the presence of long-range hydrodynamic coupling and geometrical nonlinearities. Secondly, the quantitative characterization of the filament profiles shed some light on the discontinuity in the force–torque relation.

3.1. Experimental setup

As already described in [8], we used an elastomeric filament attached to an electric motor, immersed in pure glycerin. The filament was made by filling a glass capillary tube with a 1:1 mixture of polyvinylsiloxane polymer and curing agent. Iron carbonyl particles were added to the polymer solution in order to match the density of the glycerin. The curing is thermally activated and occurs within minutes at room temperature. The glass capillary was then broken in order to retrieve an elastomeric rod of radius $a = 435\ \mu$m. The Young's modulus of the charged filament was measured by dynamical mechanical analysis: $E = 0.7$ MPa. The filament was then immersed in the glycerin tank (measuring $20 \times 20 \times 20$ cm^3). The shear viscosity $\eta = 1$ Pa s was measured with a controlled stress rheometer in a cone-plane geometry prior to each experiment, and exhibited no change due to pressure or hygroscopic variations. The motor, placed on top of the tank, could deliver discrete rotation speeds ranging from 0.01 to 10 rpm, through a gearbox, yielding Sperm numbers varying over five decades (from 10^{-1} to 10^4). The elastic filament was attached to the motor axis, so as to be fully immersed in the glycerin, with an angle $\psi = 15°$ between the filament at rest and the vertical rotation axis. Importantly, in order to

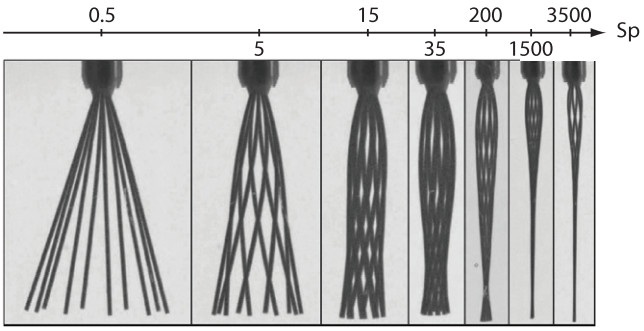

Figure 4. Evolution of the filament shape as a function of Sp. Each picture is a superposition of snapshots taken over one rotation period, with a constant time interval. As Sp increases, the filament wraps itself around and collapses on the rotation axis.

keep the anchoring condition unchanged for all experiments, the length of the filament, L, was varied from 10 to 2 cm by successively cutting the filament attached to the motor axis. The high viscosity of the fluid allowed us to remain in low Reynolds number conditions ($Re < 10^{-2}$) throughout the range of lengths and speeds available.

The filament first goes through a transient regime, which lasts up to about 1 h for the longest filament. It then reaches, as expected, a stationary shape which undergoes rigid body rotation. We here focus our attention only on the steady-state regime. Typical pictures are displayed in figure 4. To obtain the experimental shapes, a mirror was positioned with a 45° angle from the side of the tank, allowing us to take pictures of the filament projected simultaneously in two perpendicular planes with a single 6 megapixel digital camera (Nikon D70). We used a correlation algorithm to extract the coordinates from these pictures, thus determining the experimental profile with submillimeter precision.

3.2. Force and shape transitions

For all accessible Sperm numbers, we have computed the axial forces and torques F_z and T_z from quantitative image analysis, using equations (1) and (5) and $\mathbf{v}(z) = \omega r(z)\mathbf{e}_\theta$ for the local filament velocity. In figure 5 we compare our measurements to the theoretical prediction for the variations of F_z with T_z. This prediction is in qualitative agreement with the experimental data. However, we further conformed our model to the experimental data by taking into account the slight eccentricity of the anchoring point with respect to the rotation axis, $r(0) \equiv \delta_o = 2$ mm (see the pictures in figure 4). The agreement between the new prediction and the experimental data is then quantitative up to $Sp \sim 300$ and still very good for larger values of Sp (thick line in figure 5). This excellent agreement demonstrates that both the long-range hydrodynamic interactions and the geometrical nonlinearities only weakly affect the propulsive force–torque characteristics. Note that for nonzero eccentricities the asymptotic behaviors for the axial force and torque are changed in the large Sp limit, as another length scale, δ_o, is introduced. When l_ω becomes lower than δ_o, the transverse characteristic length of the helix becomes of order δ_o. As a consequence, the

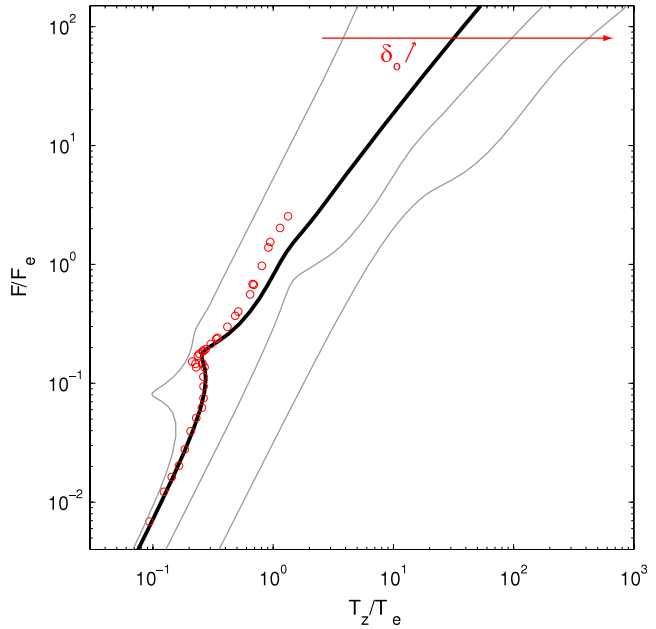

Figure 5. Normalized propulsive force F_z/F_e versus normalized axial torque T_z/T_e (case B). Thick solid line: theoretical prediction from the linear model with boundary condition $\delta_o = 2$ mm. Thin solid lines: theoretical predictions from the linear model with boundary conditions $\delta_o = 0$, $\delta_o = 10$ mm and $\delta_o = 40$ mm, from left to right. Circles: experimental data. Note that, for small eccentricities, F_z can experience an amplification by a factor of two when T_z jumps from the low-speed to the high-speed stable branch. More surprisingly, the propulsive force is lowered by almost a decade when the torque jumps from the high-speed to the low-speed stable branch.

force and torque scale as $F_z \sim \eta\omega l_\omega \delta_o \sim Sp^{3/4}$ and $T_z \sim \eta\omega l_\omega \delta_o^2 \sim Sp^{3/4}$. Remarkably, we also found that high eccentricities kill the unstable branch in the force–torque relation [14] (see the force–torque characteristics plotted for different values of δ_o in figure 5). This strong dependence on the boundary conditions was quite unexpected, and prevents us from providing a simple qualitative explanation for the existence of a first order transition in the force response.

We now come to a more detailed description of the shape transition underlying this force–torque constitutive relation. As depicted in figure 4, for $Sp < 10$ the filament remains almost straight. For intermediate Sperm numbers, $Sp \sim 10$, the filament is increasingly bent by the viscous flow, and it continuously wraps itself around the axis of rotation as Sp increases. Finally, above $Sp \sim 500$, the rod has completely collapsed on the axis but for a small fraction of the filament, below the anchoring point, which keeps its helical shape. To better characterize the collapse and the wrapping of the filament on the z axis, we display in figure 6 the evolution of the distance to the axis of the rod free end normalized by the rod length, $\delta = r(L)/L$, and of the wrapping angle, $\delta\theta = \theta(L) - \theta(0)$ (see figure 2 for the definition of θ). δ decreases monotonically as Sp increases. At low Sperm numbers, the bending of the filament mostly occurs in the flow direction and δ weakly deviates from $\sin\psi$. Indeed only chiral rods can experience forces pointing towards the rotation axis when

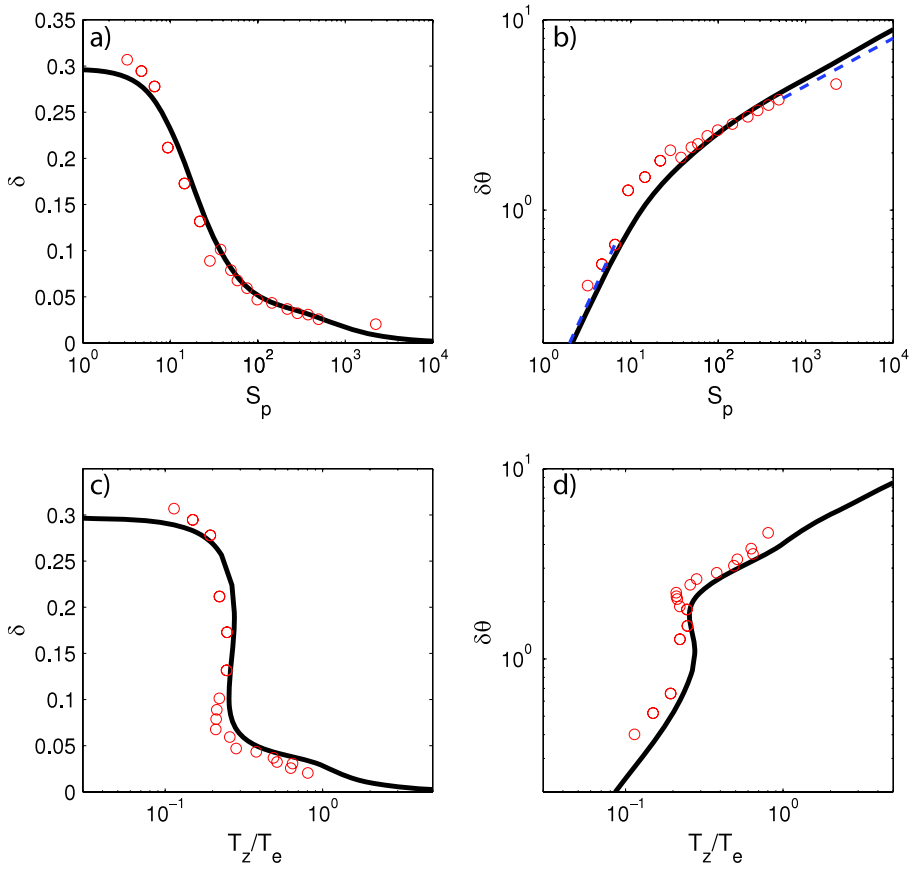

Figure 6. (a) Distance to the axis at the rod end, $\delta = r(L)/L$, as a function of Sp. (b) Wrapping angle $\delta\theta$ as a function of Sp. (c) δ as a function of the normalized actuation torque T_z/T_e. (d) $\delta\theta$ as a function of T_z/T_e. Solid lines: theoretical predictions from the linear model with boundary condition $\delta_o = 2$ mm. Circles: experimental data. Dashed lines in (b): asymptotic scaling behaviors— $\delta\theta \sim Sp$ and $\delta\theta \sim Sp^{1/4}$ in the low and high Sp limits, respectively.

undergoing a rigid body rotation, due to the symmetries of the Stokes equation upon time and parity transformations. As a consequence, whereas the orthoradial deformations scale as Sp, the bending amplitude in the radial direction must scale as Sp^2, which yields $\delta = \sin\psi - O(Sp^2)$ in the low Sp limit. For large Sperm numbers, the bending waves propagating along the filament are damped exponentially. Thus δ also decays exponentially to zero. It is important to notice that the inflexion between these two asymptotic behaviors occurs at $Sp \sim 20$, which corresponds to the onset of the unstable branch in the (T_z, F_z) constitutive relation.

The wrapping around the rotation axis increases monotonically with Sp. In the low Sp limit, the linear variations of the orthoradial bending deformations yield a linear increase of $\Delta\theta$ with Sp. Again, at $Sp \sim 20$, this linear variation crosses over to another power law regime. In this high Sp limit, we observe that $\delta\theta$ is well approximated by $Sp^{1/4}$.

The variations of δ and of $\delta\theta$ as a function of the axial torque are presented in figures 6(c) and (d). These two characteristics display an unstable branch, which would imply a discontinuous shape transition in a torque-driven experiment. When T_z exceeds the first 'critical' torque above which the rod dynamics becomes unstable the distance to the axis is lowered by more than 75%. The variations of the wrapping angle are even more spectacular: the discontinuous winding of the filament corresponds to a jump of about 70° around the rotation axis.

4. Conclusion

In this paper we have studied theoretically and experimentally the periodic motion of a flexible filament immersed in a viscous fluid. We paid special attention to the nonlinear force–torque relation resulting from the interplay between the linear elasticity of the rod and the linear Stokes flow. We have shown that the characteristics of the propulsive force strongly depends on the actuation mode for a torque-driven beating. In particular, in the case of an axial crankshafting actuation, we have identified and characterized a discontinuous transition in the filament shape resulting in a significant amplification/reduction of the propulsive force for minute variations of the imposed torque. This jump in the force would allow a microswimmer or a micropump to achieve strong accelerations without having to provide significant changes in the actuation mechanism.

Acknowledgments

This work has been partly supported by a BQR ESPCI and a DGA-CNRS fellowship (Naïs Coq).

References

[1] Bray D 2000 *Cell Movements* (New York: Garland)

[2] Lauga E 2007 Floppy swimming: viscous locomotion of actuated elastica *Phys. Rev.* E **75** 041916

[3] Lighthill J 1976 Flagellar hydrodynamics—The John von Neumann lecture 1975 *SIAM Rev.* **18** 161–230

[4] Dreyfus R, Baudry J, Roper M L, Fermigier M, Stone H A and Bibette J 2005 Microscopic artificial swimmers *Nature* **437** 862–5

[5] Manghi M, Schlagbergerand X and Netz R 2006 Propulsion with a rotating elastic nanorod *Phys. Rev. Lett.* **96** 068101

[6] Vilfan A and Jülicher F 2006 Hydrodynamic flow patterns and synchronization of beating cilia *Phys. Rev. Lett.* **96** 058102

[7] Qian B, Powers T and Breuer K 2008 Shape transition and propulsive force of an elastic rod rotating in a viscous fluid *Phys. Rev. Lett.* **100** 078101

[8] Coq N, du Roure O, Marthelot J, Bartolo D and Fermigier M 2008 Rotational dynamics of a soft filament: wrapping transition and propulsive forces *Phys. Fluids* **20** 051703

[9] Wiggins C H and Goldstein R E 1998 Flexive and propulsive dynamics of elastica at low Reynolds number *Phys. Rev. Lett.* **80** 3879–82

[10] Yu T S, Lauga E and Hosoí A E 2006 Experimental investigation of elastic tail propulsion at low Reynolds number *Phys. Fluids* **18** 091701

[11] Batchelor G K 1970 Slender-body theory for particles of arbitrary cross-section in stokes flow *J. Fluid Mech.* **44** 419

[12] Machin K E 1958 Wave propagation along flagella *J. Exp. Biol.* **35** 796

[13] Hulin J-P, Guyon E, Petit L and Mitescu C D 2001 *Physical Hydrodynamics* (Oxford: Oxford University Press)

[14] Coq N, unpublished result